Photofragmentation dynamics of N,N-dimethylformamide following excitation at 193 nm

M. Laura Lipciuc[1], Sara H. Gardiner[1], Tolga N. V. Karsili[2], Jason W. L. Lee[1], David Heathcote[1], Michael N. R. Ashfold[2], and Claire Vallance[1]

[1] *Department of Chemistry, University of Oxford, Chemistry Research Laboratory, 12 Mansfield Road, Oxford OX1 3TA, UK*

[2] *School of Chemistry, University of Bristol, Cantocks Close, Bristol BS8 1TS, UK*

Corresponding author e-mail: claire.vallance@chem.ox.ac.uk

Abstract

N,N-dimethylformamide, $HCON(CH_3)_2$, is a useful model compound for investigating peptide bond photofragmentation dynamics. We report data from a comprehensive experimental and theoretical study into the photofragmentation dynamics of N,N-dimethylformamide in the gas phase at 193 nm. Through a combination of velocity-map imaging and hydrogen atom Rydberg tagging photofragment translational spectroscopy, we have identified two primary fragmentation channels, namely fission of the N−CO 'peptide' bond, and N−CH_3 bond fission leading to loss of CH_3. The possible fragmentation channels leading to the observed products are rationalised with recourse to CASPT2 calculations of the ground and first few excited-state potential energy curves along the relevant dissociation coordinates, and the results are compared with data from previous experimental and theoretical

studies on the same system.

1 Introduction

Photofragmentation studies on amide systems are of key interest as a stepping stone to understanding the behaviour of energised peptide bonds within proteins. In addition to providing insight into photostability and photodamage mechanisms in biomolecules, such studies also have the potential to inform mass spectrometric studies of molecular structure, in which UV photolysis is increasingly being used to induce fragmentation [1]. The present study focuses on the 193 nm photofragmentation of N,N-dimethylformamide (N,N-DMF), a molecule that has been considered previously in a number of experimental[2, 3] and theoretical[4, 5] studies as a useful model compound for investigating peptide bond fragmentation dynamics. In common with peptide bonds in proteins, N,N-DMF has a planar structure (see Figure 1), as a consequence of the partial double bond character of the N−CO 'peptide' bond that results from partial conjugation of the lone pair on the nitrogen atom into the C=O π^* system.

The long wavelength part of the UV absorption spectrum of N,N-DMF shows two overlapping bands, peaking at 197.4 nm and 162.1 nm, respectively. Previous theoretical studies have identified singlet states attributable to $\pi^* \leftarrow n$ transitions in which an oxygen $2p_y$ lone-pair electron and a nitrogen $2p\pi$ lone-pair electron, respectively, are promoted to the C=O π^* antibonding orbital [6, 7, 8, 9]. The photolysis wavelength of 193 nm employed in the present study is close to the peak of the first of the two absorption

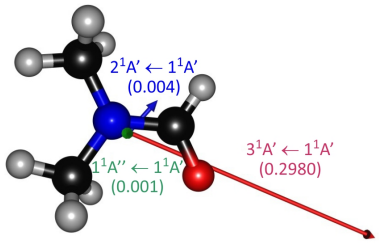

Figure 1: The molecular structure of N,N-dimethylformamide. The calculated transition dipole moments for excitation from the $1^1A'$ ground state to the $1^1A''$ (S_1), $2^1A'$ (S_2), and $3^1A'$ (S_3) states are shown as green, blue, and red arrows, respectively (see Section 2.2 for a description of these calculations).

bands. However, previous experimental studies [3, 10] have indicated that both transitions can be excited at this wavelength, and result in fragmentation of the parent molecule via cleavage of the N-CO 'peptide' bond, one of the N-CH_3 bonds, or possibly the aldehydic C-H bond.

Focusing first on the 'peptide' bond fragmentation channels accessible at 193 nm, three different pairs of electronic states are accessible on energetic grounds for the HCO + $N(CH_3)_2$ products. Both products can be formed in their ground states (i.e. HCO [$\tilde{X}$]+ $N(CH_3)_2$ [$\tilde{X}$]), or either the HCO or $N(CH_3)_2$ product can be formed in its first excited state (i.e. HCO [$\tilde{A}$] or $N(CH_3)_2$ [$\tilde{A}$]). The amount of energy available to be released into product translation is different in each case, and therefore experimental measurements of the photofragment velocity distributions offer a potential route to establishing the branching ratios for formation of each of the three possible product pairs. These in turn provide insight into the details and

topographies of the potential energy surfaces that control the fragmentation dynamics.

Forde *et al.*[2, 3] performed such a study in the late 1990s. A traditional photofragment translational spectroscopy method was employed, in which time-of-flight profiles for selected photofragments were recorded by electron ionization and quadrupole mass spectrometric detection. The authors identified contributions from three dissociation pathways following excitation at 193 nm. Two involved N-CO 'peptide' bond cleavage, leading to formation of ground-state HCO[$\tilde{\mathrm{X}}$] radicals partnered by $N(CH_3)_2$ radicals in both their $\tilde{\mathrm{X}}$ and $\tilde{\mathrm{A}}$ states. These products showed an anisotropic recoil velocity distribution, characterised by a recoil anisotropy parameter $\beta = 1.2 \pm 0.2$. This was thought to indicate prompt bond rupture relative to the parent rotational period, following excitation via a transition with an associated dipole moment aligned preferentially parallel to the breaking bond. The limited available translational energy resolution precluded determination of separate β parameters for each of the two product channels. The third dissociation pathway identified was N-CH_3 bond fission, which was estimated to account for around one third of the measured fragmentation yield. Unfortunately, problems with overlapping time-of-flight signals and interfering signals from CH_3^+ ions formed by the cracking of larger fragments within the ionization region of the detector prevented determination of the associated β parameter. The possible participation of fragmentation channels involving loss of an H atom could not be assessed on account of high background signals at this mass.

Forde *et al.* [2, 3] also reported preliminary results from *ab initio* elec-

tronic structure calculations that were performed in order to aid interpretation of their experimental data. These were followed by two further theoretical studies by Liu *et al.* [4] and Eckert-Maksić and Antol [5]. Liu *et al.* employed state-averaged complete active space self-consistent field (SA-CASSCF) methods to compute the ground (S_0) and first excited singlet (S_1) and triplet (T_1) adiabatic potential energy surfaces of N,N-DMF and the regions of configuration space in which these surfaces intersect. They concluded that most of the N-CO 'peptide' bond cleavage following excitation at 193 nm occurs on the S_1 surface, with some contribution from the T_1 surface following intersystem crossing (ISC) from S_1, both leading to the formation HCO and $N(CH_3)_2$ products in their electronic ground states. The triplet state was also thought to dissociate along a CH_3-loss coordinate to give $HCONCH_3$ + CH_3 products. The later study by Eckert-Maksić and Antol [5] employed similar SA-CASSCF calculations to locate stationary points (energy minima and saddle points) and minima on the crossing seams linking the S_0, S_1, and S_2 surfaces. These were then used in direct trajectory surface hopping calculations to explore possible routes to 'peptide' bond fission following 193 nm photoexcitation of N,N-DMF. We will explore the conclusions reached in these various theoretical treatments in Section 3.

In the present work, we report a new experimental study of the 193 nm photofragmentation dynamics of N,N-dimethylformamide employing 'universal' vacuum ultraviolet (VUV) photoionization and velocity-map imaging of the resulting photofragments. The velocity-map images provide much higher angular resolution than the earlier photofragment translational spec-

troscopy measurements of Forde *et al.* [2, 3], though these measurements were state-of-the-art for their time. The present imaging studies are also less prone to complications associated with the overlap of time-of-flight signals from different ion masses. The much lower ionization energy employed in our experiments (a 10.48 eV laser photon rather than a 200 eV electron) also circumvents many of the challenges associated with cracking of photofragments into smaller species at the detector, allowing better reconstruction of the signals for intact photofragments. Possible hydrogen atom elimination channels have also been investigated via separate hydrogen Rydberg atom photofragment translational spectroscopy measurements. Analysis of the time-of-flight spectra and photofragment translational energy and angular distributions extracted from the data, supported by new *ab initio* calculations of the energetic pathways for the energetically accessible fragmentation processes, allows us to revisit the earlier conclusions drawn by Forde *et al.* [2, 3], to confirm many of their findings, and to address some of the open questions posed by their work and the theoretical studies that followed.

2 Methods

2.1 Experiment

The velocity-map imaging experimental setup has been described in detail elsewhere [11, 12]. The following is a brief description of the experimental conditions. A seeded beam (seeding ratio ∼0.2%) of ∼4 mbar N,N-dimethylformamide (Sigma-Aldrich, >99.8%) in 2 bar of He (BOC, > 99.9%) undergoes a supersonic expansion through a pulsed solenoid valve

(Parker Hannifin, Series 9) into vacuum to generate the molecular beam. Within the interaction region, the molecular beam is intersected at right angles by two counter-propagating linearly-polarized laser beams of wavelengths 193 nm (from a Neweks PSX-100 ArF excimer laser) and 118.2 nm (generated by tripling the 355 nm output of a Continuum Surelite I Nd:YAG laser in a phase-matched mixture of Xe and Ar[13, 14, 15]), separated in time by about 20 ns. The N,N-DMF molecules are photolysed by a 193 nm photon, and the resulting neutral dissociation products are ionized by a VUV photon. The nascent ions are velocity-mapped along a 48.2 cm flight tube onto a position sensitive detector (Photonis) consisting of a pair of microchannel plates coupled to a P47 phosphor screen. The microchannel plates are time-gated to the arrival time of the ion of interest using a high-voltage pulse generator (Photek GM-MCP-2), and images from the phosphor are acquired with an intensified CCD camera (Photonic Science MiniIDI) via a LabVIEW interface. Images are accumulated over several tens of thousands of laser pump-probe cycles in order to achieve an acceptable signal-to-noise ratio. Time-of-flight mass spectra are recorded by counting the number of ions detected as a 20 ns time-gate applied to the microchannel plates is swept across the ion arrival time range of interest. Time-of-flight spectra and velocity-map images are recorded for pump-only, probe-only, and pump-probe laser combinations, and the single-laser signals are subtracted from the two-laser signal to give the true pump-probe signal, corresponding to photofragments generated by the 193 nm photolysis that are then ionized by the 118 nm probe laser. The assignment of the various peaks in the time-of-flight spectra was confirmed by recording similar spec-

tra for N,N-DMF-d7 and observing the expected changes in mass-to-charge ratio for each fragment.

The images were processed using the BASEX software package [16] in order to obtain the speed and angular distributions of the various photofragments. The measured product velocities were calibrated using images of atomic oxygen atoms of known velocity produced in the multiphoton dissociation and ionization of molecular oxygen at 225 nm [17].

In order to investigate hydrogen loss channels from N,N-DMF, H-atom Rydberg Tagging measurements have been performed. The instrument has been described in detail previously [18]. In brief, a pulsed molecular beam comprising N,N-DMF (Sigma Aldrich, >99%, room temperature vapour pressure) in ∼1 bar of Ar was expanded through a pulsed valve and skimmed prior to photolysis at 193 nm. H atoms formed in this interaction region were probed by two-photon (121.6 nm + 366 nm) double resonant excitation *via* the *2p* state to a high n Rydberg state. Rydberg atoms that recoil along the axis orthogonal to the plane containing the molecular beam and the photolysis/probe laser beams traverse a flight tube to a detector, where their times-of-flight are recorded. An extraction field of 50 Vcm^{-1} applied across the interaction region ensures prompt removal of any H^+ ions created in the interaction region.

We note that in both sets of experiments we were able to obtain sufficiently high signal levels with a relatively low concentration of N,N-DMF within the molecular beam, in contrast to the much higher concentrations of around 8% employed by Forde *et al.*[3]. We saw no significant evidence of clustering within the beam, and did not need to heat the pulsed valve to

prevent clusters from interfering with the signal from monomer fragmentation. The molecules undergoing photofragmentation in the present study are therefore likely to be significantly colder than in the previous experimental study of Forde *et al.*

2.2 Computational Methodology

The ground-state optimized geometries and energies of neutral N,N-DMF and the various fragmentation products were obtained at the MP2/aug-cc-pVTZ level using the Gaussian09 software package [19]. In accord with the earlier studies discussed in Section 1, products corresponding to N−CO 'peptide' bond fragmentation, CH_3 loss, and H-loss are all deduced to be energetically accessible at this wavelength.

Further calculations were performed using the MOLPRO Version 2010.1 computational package[20]. Using the MP2 optimised parent molecule geometry, vertical excitation energies and transition dipole moments for various neutral states of N,N-DMF were calculated using a state-averaged CASSCF method, employing the same aug-cc-pVTZ basis set as the initial geometry optimisations. The calculated transition dipole moments for vertical excitation to the $1^1A''$, $2^1A'$, and $3^1A'$ states are superimposed on the molecular structure for N,N-DMF shown in Figure 1.

The choice of active space was a balance between attempting to describe all significant static correlation effects in the ground and excited electronic states in as even-handed a way as possible across the potential energy surface, and constraining the calculation to a manageable size. The active space comprised 12 electrons arranged in nine orbitals, namely three σ and

two σ^* orbitals, the in-plane oxygen p_y orbital, π and π^* orbitals centered around the C=O bond, and the nitrogen p_x orbital. Individual potential energy curves (PECs) along the N−CO 'peptide', methylamino N−CH_3, and aldehydic C−H stretching coordinates were calculated at CASPT2 level for the ground and various excited electronic states of the N,N-DMF neutral molecule. In each case, the remainder of the nuclear framework was frozen at the ground-state optimised geometry as the active coordinate was varied. A small imaginary level shift of 0.5 a.u. was applied to encourage convergence and to circumvent the presence of intruder states. Vertical excitation energies obtained from the CASPT2 calculations are in good agreement with the available experimental data [6, 7].

In addition to the potential energy surface calculations outlined above, vertical ionization energies for the various relevant molecular fragments were calculated at the HF/aug-cc-pVTZ level with P3 electron propagator theory correlation correction. These are shown in Table 1, and will be used to rationalise the presence or absence of signals from the various possible photolysis products following irradiation with 193 nm pump and 118 nm (10.48 eV) probe radiation.

3 Results and Discussion

3.1 Potential energy curves

Cuts through the CASPT2 potential energy surfaces calculated along (a) the N−CO bond, (b) a N−CH_3 bond, and (c) the aldehydic C−H stretch coordinate are shown in the three panels of Figure 2. The vertical excitation

Table 1: Vertical ionization energies for the photolysis products of N,N-dimethylformamide, calculated at HF/aug-cc-pVTZ level with P3 electron propagator theory correlation correction.

Species	Vertical ionization energy / eV	Ionizable at 193 nm?	Ionizable at 118 nm?
$HCON(CH_3)_2$	9.59	No	Yes
$CON(CH_3)_2$	7.82	No	Yes
$HCONCH_3$	11.32	No	No
$N(CH_3)_2$	9.89	No	Yes
NC_2H_5	9.90	No	Yes
cis-$NCHCH_3$	7.93	No	Yes
trans-$NCHCH_3$	7.59	No	Yes
NH_4	4.44	Yes	Yes
CH_3	9.79	No	Yes
HCO	8.83	No	Yes
CO	13.79	No	No
H	13.60	No	No

energies to the first three singlet excited states, namely the $1^1A''$, $2^1A'$ and $3^1A'$ states, are ∼5.0, ∼6.0 and ∼6.0 eV, respectively. All three states are therefore energetically accessible following absorption of a 6.42 eV photon of 193 nm light. The calculated vertical excitation energy to the $1^1A''$ state is lower than that reported by Eckert-Maksić and Antol[5], but still well above their reported value for the adiabatic transition to the (non-planar, trans-isomer) minimum energy geometry of the S_1 state. In accord with previous findings, the dominant orbital promotion associated with the $1^1A'' \leftarrow S_0$ transition in the Franck-Condon region is best described as $\pi^* \leftarrow n_O$. The $2^1A'$ and $3^1A'$ states returned by the present calculations are near degenerate; the former has 3s Rydberg character, while the latter arises as a result of $\pi^* \leftarrow \pi$ excitation. The very different spatial overlaps of the participating orbitals are reflected in the calculated oscillator strengths for the respective transitions from the S_0 state to the $1^1A''$, $2^1A'$ and $3^1A'$ states (0.001, 0.004 and 0.298, respectively). Thus, in contrast to the previous literature [5], we identify the $3^1A'$ state as the 'bright' $^1\pi\pi^*$ state. However, we recognise that this state is likely to be heavily mixed with, and predissociated by, the $2^1A'$ state, and that nuclear motions on the latter potential energy surface will drive the fragmentations of current interest.

Focussing on the N−CO bond fission channel first, the potential energy curves in Figure 2(a) show several curve crossings which develop into conical intersections once the planarity constraint is lifted. The calculated oscillator strengths imply predominant excitation to the $3^1A'$ state of N,N-DMF following excitation at 193 nm, but as noted above we envisage rapid population transfer to the $2^1A'$ state. The $2^1A'$ state correlates with the first

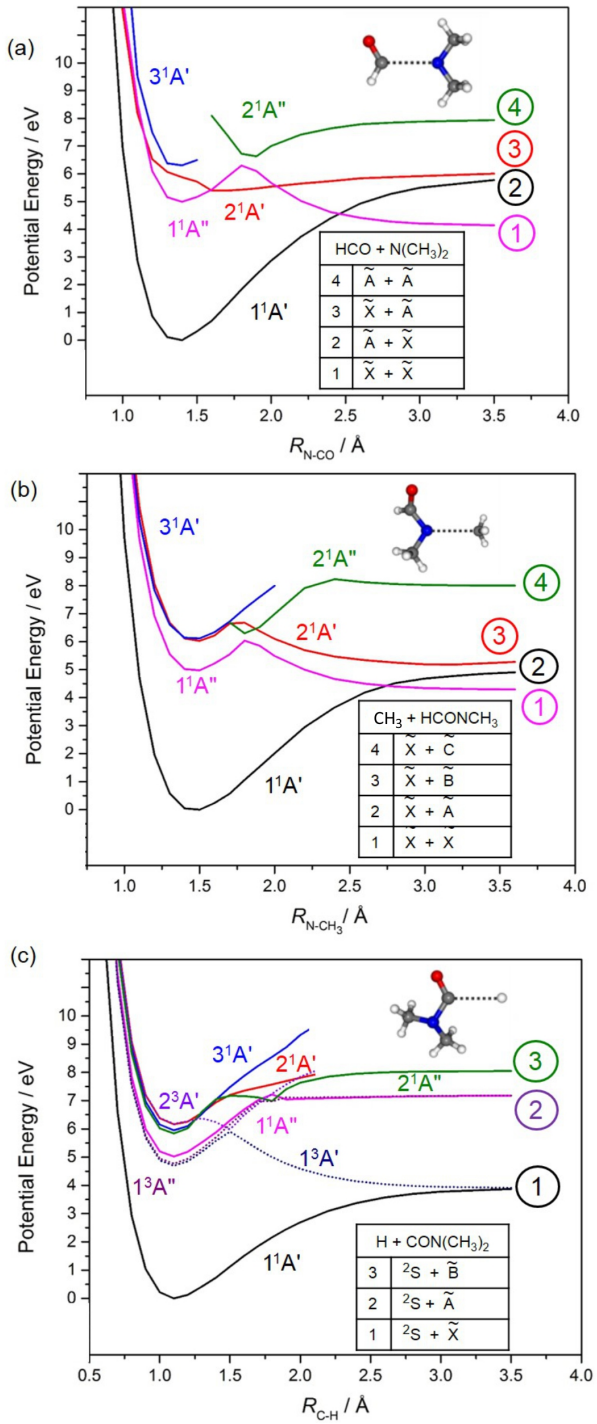

Figure 2: Cuts through the adiabatic potential energy surfaces returned from CASPT2 calculations for dissociation of N,N-DMF along the (a) $R_{\mathrm{N-CO}}$, (b) $R_{\mathrm{N-CH_3}}$, and (c) aldehydic $R_{\mathrm{C-H}}$ bond extension coordinates. All other degrees of freedom were held fixed at their ground state equilibrium values during the calculations.

excited state of the $N(CH_3)_2$ radical upon N−CO bond extension. However, at extended N−CO bond lengths of around 2Å, population on the $2^1A'$ surface can also couple to the repulsive $1^1A''$ potential, which correlates to ground-state products. The long-range part of this $1^1A''$ potential arises as a result of excitation from the delocalised π orbital spanning the nitrogen $2p_x$ orbital and C=O bond to a σ^* orbital localised along the N−CO bond. The potential energy curve for the resulting $^1\pi\sigma^*$ state shows a topography reminiscent of that of many other $(n/\pi)\sigma^*$ states[21], even that for N−H bond fission in NH_3. In the planar limit, the state correlates asymptotically with ground-state products. However, a conical intersection with the $1^1A'(S_0)$ potential energy curve at $R_{N-CO} \sim 2.5$ Å has the result that any loss of planarity, for example by pyramidalisation at the N atom, would favour dissociation to electronically excited HCO products. Parent molecules initially excited to the $1^1A''$ state are likely to follow a similar sequence of radiationless transitions to those excited to the $2^1A'$ or $3^1A'$ states after initial coupling to the $2^1A'$ state via another conical intersection at shorter R_{N-CO} distances.

The calculated potential energy curves along the $N-CH_3$ stretch coordinate (Figure 2(b)) show some similarities to those along the N−CO coordinate. Again, the curves for the $1^1A''$ and $2^1A'$ states correlate to excited dissociation limits, in this case associated with formation of electronically excited $HCONCH_3$ radicals. The $2^1A'$ curve shows a barrier at $R_{N-CH_3} \sim 1.75$ Å, which we ascribe to the lower half of an avoided crossing with another state of $^1A'$ symmetry. The barrier height is almost certainly overestimated in the present (unrelaxed) calculations, so we can expect that

$N-CH_3$ bond fission is adiabatically allowed following excitation to the $3^1A'$ state at 193 nm and subsequent coupling to the $2^1A'$ potential. The $1^1A''$ and $2^1A'$ potential energy curves are both intersected at planar geometries by the repulsive part of the $1^1A''$ curve. The dominant orbital promotion associated with this dissociative region of the potential is from the same π orbital delocalised over the N-C=O spine as identified earlier to another σ^* orbital, this time localised along one $N-CH_3$ bond. The resulting state offers another possible fragmentation pathway for population in the $2^1A'$ state, initiated by radiationless coupling (induced by an appropriate out-of-plane motion) at the conical intersection between the $2^1A'$ and $1^1A''$ states at $R_{N-CH_3} \sim 1.7$ Å. As was the case for dissociation along the $N-CO$ coordinate, the $1^1A''$ potential energy curve forms a conical intersection with the S_0 curve at extended $N-CH_3$ bond lengths of ∼2.75 Å. As noted earlier, this is reminiscent of the $(n/\pi)\sigma^*$-state-mediated dissociation [21] of NH_3 or CH_3NH_2. Dissociating N,N-DMF molecules following this pathway can either form ground-state radical products, if the last conical intersection is sampled at near planar geometries, or CH_3 + $HCONCH_3[\tilde{A}]$ products if the adiabatic path (for non-planar geometries) is followed at the conical intersection.

Unlike the potential energy curves along the $N-CO$ and $N-CH_3$ stretching coordinates, the singlet curves for the aldehydic $C-H$ bond extension coordinate do not show a low-energy conical intersection at extended bond lengths, and instead are more reminiscent of simpler systems such as H_2CO and HFCO [22, 23, 24, 25]. The only dissociative potential energy curve along this coordinate is that of a $^3A'$ triplet state, formed by promoting an

electron to a σ^* orbital localised on the breaking C−H bond. The importance of this channel will depend on the strength of the spin-orbit coupling from the photoexcited $1^1A''$, $2^1A'$, and/or $3^1A'$ states to the triplet manifold.

Continuing the analogy with H_2CO and HFCO suggests that we should also be cognisant of a possible molecular fragmentation channel yielding $(CH_3)_2NH$ + CO products. These are in fact the lowest energy dissociation products that could arise from photolysis of N,N-DMF [2, 3], but their formation would certainly involve passage over a substantial activation barrier. This pathway has not been investigated in the present computational work, but we note that the 8.24 eV ionization energy of the $(CH_3)_2NH$ product [26] is sufficiently low that any activity in this channel should be revealed by the present experiments.

3.2 Time-of-flight mass spectra and velocity-map images

Time-of-flight mass spectra were recorded for the photofragments generated following illumination of the sample by (a) only the 193 nm pump (UV) light,(b) only the 118 nm probe (VUV) light, and (c) both the 193 nm pump and 118 nm probe (UV/VUV) light. These spectra are shown in Figure 3(a). The only signal generated by the pump laser alone is a small peak at $m/z = 44$, corresponding to one-photon fragmentation of the peptide bond followed by two-photon non-resonant ionization of the $N(CH_3)_2$ product within the same laser pulse. Single-photon ionization can be ruled out on the basis that with a calculated vertical ionization energy of 9.89 eV, the total energy available to the photolysis products is insufficient for even the most highly internally excited $N(CH_3)_2$ products to be ionized by a single photon at

193 nm. The probe laser alone generates a large peak at the parent ion mass, $m/z = 73$, together with peaks at $m/z = 30$, 42, 44, 58, 70, and 72 corresponding to dissociative ionization products. These can be assigned as $C_2H_6^+$, $NC_2H_4^+$, $N(CH_3)_2^+$, $HCONCH_3^+$, and various H-atom-loss products, respectively.

When the sample is illuminated by both the pump and probe lasers, new peaks appear at $m/z = 15$, 18, 28, and 29. In addition, the peaks assigned above to probe-laser dissociative ionization are all attenuated, since neutral dissociation of N,N-DMF by the pump laser reduces the number of parent molecules available to undergo dissociative ionization. The true pump-probe signal, generated when neutral products of 193 nm laser photolysis are subsequently ionized by the 118 nm probe laser, is found by subtracting the 'pump-only' and 'probe-only' signals from the pump-probe signal, and is shown in Figure 3(b). The products of parent molecule dissociative ionization appear as negative peaks, due to the previously noted attenuation of these signals when some of the parent molecules are dissociated by the 193 nm pump laser. The pump-probe signals of interest appear as positive peaks at m/z=15, 18, 28, 29, 42, and 43. The corresponding velocity-map images, with pump-only and probe-only 'background' signal already subtracted, are shown in Figure 4, along with the speed distributions and velocity-dependent recoil anisotropy parameters, $\beta(v)$ extracted from the images. Values for β averaged over the velocity distribution for each fragment are shown in Table 2.

As noted previously, following absorption of a 193 nm photon, N,N-dimethylformamide is expected to dissociate via cleavage of either the N−CO

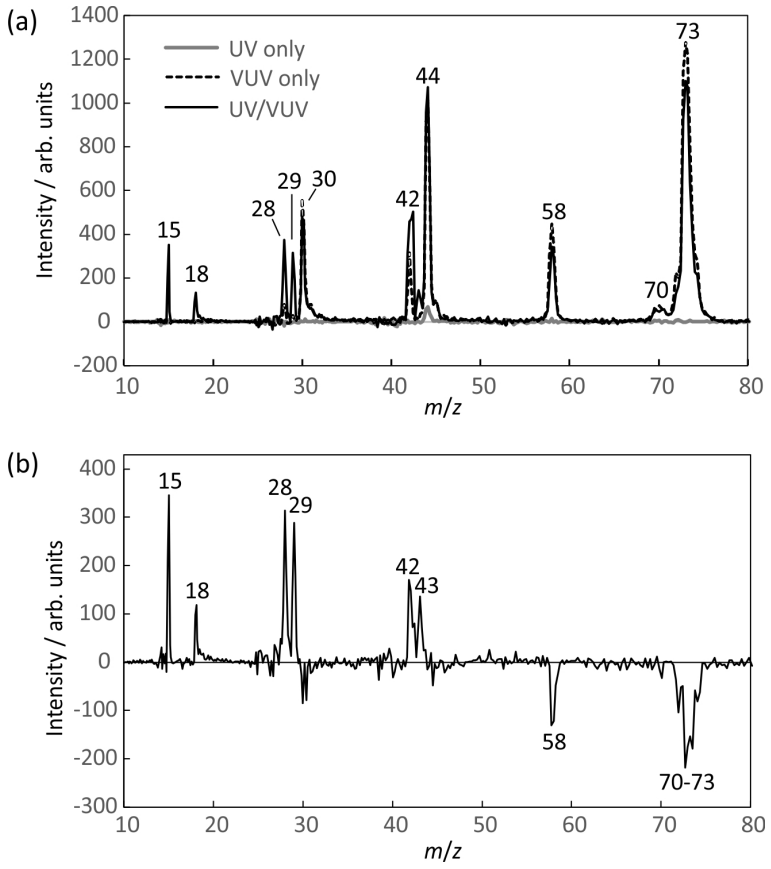

Figure 3: (a) Time-of-flight mass spectra recorded with 118 nm pump only, 193 nm probe only, and with pump and probe lasers; (b) background subtracted time-of-flight spectrum showing the true two-colour pump-probe signal. See text for detailed discussion.

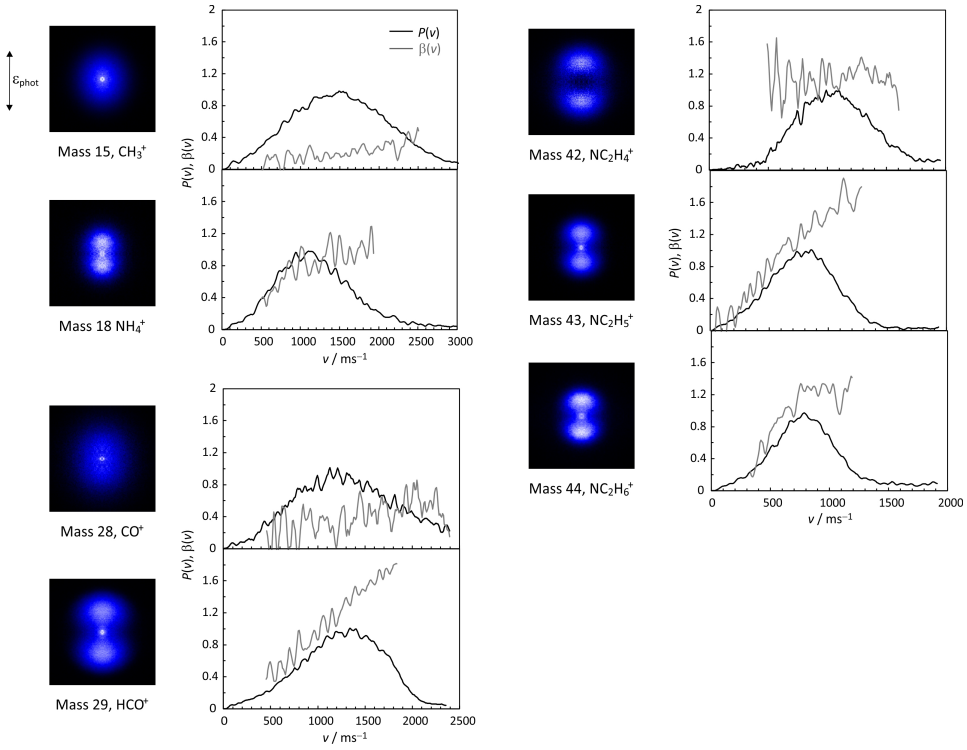

Figure 4: Top: Background-subtracted velocity-map images for the fragments with m/z = 15,18,28,29,42, and 43, and one-laser velocity-map image for the $m/z = 44$ fragment, together with the corresponding speed distributions $P(v)$ and velocity-dependent recoil anisotropy parameters, $\beta(v)$. Speed distributions have been normalised to a peak value of unity.

'peptide' bond, an N−CH_3 bond, or the aldehydic C−H bond. We consider each of these in turn in light of the data presented in Figures 3 and 4 and the potential energy curves presented in Section 3.1.

Table 2: Beta parameters averaged over product speed distribution. Estimated uncertainties in the last two digits based on one standard deviation of the difference between $\beta(v)$ (plotted in Figure 4) and a polynomial fit through the data are given in parentheses.

Species	m/z	β
CH_3^+	15	0.19(07)
NH_4^+	18	0.76(15)
CO^+	28	0.34(16)
HCO^+	29	1.19(08)
$NC_2H_4^+$	42	1.05(16)
$NC_2H_5^+$	43	1.12(12)
$N(CH_3)_2^+$	44	0.92(09)

3.3 N-CO 'peptide' bond cleavage

As summarised in Section 1, previous experimental and theoretical studies of N,N-DMF photolysis [3, 4, 5] have proposed several pathways for cleavage of the N-CO 'peptide' bond, leading to formation of HCO and $N(CH_3)_2$ products in various combinations of their ground and first-excited electronic states. Following cleavage of the N−CO bond, we therefore expect to observe signals in the time-of-flight mass spectrum corresponding to the HCO and $N(CH_3)_2$ products at $m/z = 29$ and 44. Unfortunately, the situation is a

little more complicated than this due to neutral dissociation of a portion of the nascent HCO fragments and dissociative ionization of the $N(CH_3)_2$ fragments. However, we can still piece together the signals arising from this pathway. As noted previously, in the absence of the 118 nm laser we observe a small signal at $m/z = 44$, attributed to $N(CH_3)_2$ products of N−CO bond cleavage that have been ionized by further photons from the 193 nm pump laser. The velocity-map image for these fragments is shown in Figure 4, and exhibits strong alignment of the product velocities parallel to the laser polarisation axis. The velocity-averaged recoil anisotropy parameter, β, is 0.92, but as can be seen in Figure 4, β increases steadily from small values at low velocities to almost its limiting value of +2 for the fastest fragments. A positive value of β is expected if the dissociation is rapid, given that the transition dipole moment for the (assumed) dominant $\pi^* \leftarrow \pi$ transition lies roughly parallel to the breaking N−CO bond (see Figure 1). The increase in β with photofragment velocity implies that while the axial recoil approximation holds for the fragments formed with the highest kinetic energy releases, it breaks down for slower fragments, reducing the value of β. This will be discussed in more detail later.

The $m/z = 44$ image discussed above was recorded with 193 nm pump radiation alone. Upon introduction of the 118 nm probe laser, the signal at m/z=44 disappears, and instead, signals associated with the N−CO dissociation pathway can be identified at $m/z = 18$, 28, 29, 42, and 43. Based on the masses, ionization energies of the corresponding neutrals, and velocity-map images, the signals at $m/z = 18$, 42, and 43 can be assigned as $NC_2H_5^+$, $NC_2H_4^+$, and NH_4^+ products of dissociative ionization of the $N(CH_3)_2$ frag-

ment, while the HCO^+ fragment appears at $m/z = 29$. The energetics preclude the observed CO^+ ions at $m/z = 28$ being dissociative ionization products of HCO, and as we will discuss below, we believe instead that a portion of the more internally excited neutral HCO fragments undergo neutral dissociation to H + CO, whereby a portion of the CO is ionized by a combination of 193 nm and 118 nm photons.

We consider first the $N(CH_3)_2$ fragments and their dissociative ionization products. Previous studies [27] have shown a propensity for more highly internally excited $N(CH_3)_2^+$ ions to dissociate via H-atom loss to give $m/z = 43$ daughter ions, while $N(CH_3)_2^+$ ions with less internal energy lose H_2 to yield daughter ions with $m/z = 42$. The present study appears to corroborate this finding. The velocity-map image for the $NC_2H_5^+$ fragments ($m/z = 43$) is almost identical to that for the mass 44 fragments detected in the absence of the 118 nm light. In contrast, the velocity-map image for the $NC_2H_4^+$ fragments ($m/z = 42$) corresponds to fragments with significantly higher average velocities, and therefore lower internal energies; in fact, the image has a clear 'hole' in the centre, indicating that it contains no contribution at all from the most highly internally excited products. The NH_4^+ ($m/z = 18$) fragments exhibit a similar angular distribution to that of the heavier fragments, indicating that the considerable rearrangement required for formation of NH_4^+ results in little additional kinetic energy release on dissociation.

Signal arising from the HCO co-product appears at $m/z = 29$ (HCO^+) and 28 (CO^+). The 10.48 eV energy of a 118 nm photon exceeds the 8.83 eV ionization energy of HCO, but is well below the 13.79 eV ionization energy

of CO. The observed CO^+ signal is thus unlikely to arise from neutral CO[X] products of N,N-DMF photolysis. Instead, based on the relatively low kinetic energy release revealed by the velocity-map image of the m/z 28 ions relative to the HCO^+ ions, we conclude that the observed CO^+ signal arises from predissociation of internally excited HCO products, followed by ionization of the resulting neutral CO fragments.

With a few assumptions, it is possible to reconstruct the momentum distributions of the nascent $N(CH_3)_2$ and HCO fragments from the velocity-map images of the various detected secondary fragment ions. Considering first the $N(CH_3)_2$ product, we assume that loss of H or H_2 from $N(CH_3)_2$ during the dissociative ionization process and from HCO during predissociation does not greatly affect the velocity of the remaining fragment (since the very light H or H_2 carries away the bulk of the kinetic energy associated with the dissociation), and also that there is little further kinetic energy release when $N(CH_3)_2^+$ dissociates to form NH_4^+. The sum of the velocity-map images and momentum distributions for the mass 18, 42, and 43 fragments, weighted according to the relative intensities of their time-of-flight signals, should therefore recreate the momentum distribution of the nascent $N(CH_3)_2$ fragments.

Considering now the HCO products, the relative ionization efficiencies, and therefore detection efficiencies, of the nascent HCO and its predissociation product CO are unknown. However, a suitably weighted sum of the HCO and CO momentum distributions should reproduce the momentum distribution deduced for the $N(CH_3)_2$ fragments and their dissociative ionization products. Serendipitously, it appears that the CO and HCO ion-

ization probabilities are similar under our experimental conditions, and that the best momentum matching with the $N(CH_3)_3$ fragments is obtained by summing the momentum distributions for the $m/z = 29$ and 30 fragments, again weighted simply according to the intensities of their time-of-flight signals.

The summed velocity-map images and momentum distributions are shown in Figure 5. Note that when calculating the relevant momenta, we have used the mass of the nascent HCO ($m/z = 29$) fragment to calculate the momenta associated with the $m/z = 28$ and 29 fragments, and the mass of the nascent $N(CH_3)_2$ ($m/z = 44$) fragment to calculate the momenta associated with the $m/z = 18$, 42, and 43 fragments. There is almost perfect momentum matching between the reconstructed distributions for the HCO and $N(CH_3)_2$ fragments, as should be the case for the products of a two-body dissociation. The level of agreement between the two momentum distributions serves to confirm that we have correctly identified the various fragmentation processes giving rise to the observed signals.

We will now consider in more detail the product angular and kinetic energy distributions following N−CO bond cleavage. The velocity-dependent β parameters extracted from all of the images (see Figure 4) increase with fragment velocity, approaching a limiting value of 2 for the fastest fragments detected at masses 29 and 43. The finding that β varies with recoil velocity is reminiscent of previous observations for the $H + NH_2$ products arising in the near UV photolysis studies of NH_3 [28, 29], and can be traced to the spread of out-of-plane motions in the dissociating molecules. The potential energy curves shown in Figure 2(a) and the previous studies of Eckert-Maksić and

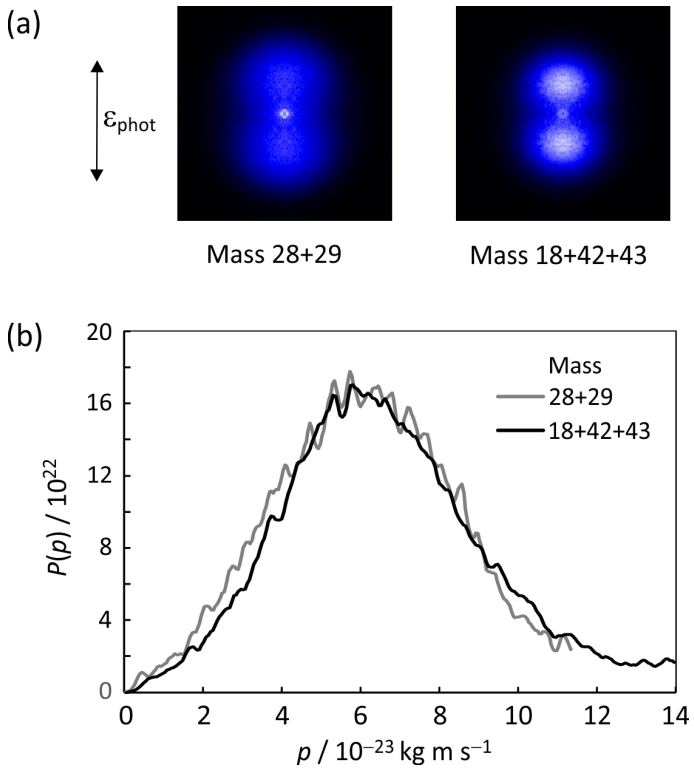

Figure 5: (a) Summed velocity-map images and (b) summed momentum distributions, $P(p)$, for the fragments arising from N−CO 'peptide' bond fission, showing almost exact momentum matching. The momentum distributions have been normalised to unit area under the curve.

Antol [5] highlight several regions where the topography of the potential energy surfaces will encourage out-of-plane motion in concert with N−CO bond extension. Initial excitation to any of the three accessible states, $1^1A''$, $2^1A'$, or $3^1A'$, each of which have non-planar minimum energy geometries, rapidly leads to population in the $1^1A''$ state via radiationless transfer first to the $2^1A'$ state and then at the $2^1A'/1^1A''$ conical intersection (TS1 in reference [5]). Accessing these conical intersections requires an out-of-plane coupling mode, as does any subsequent transfer at the $1^1A''/1^1A'$ conical intersection (MXS1 in reference [5]). Eckert-Maksić and Antol highlight the "significant reduction of pyramidalisation at the C and the N atoms of the peptide moiety at MXS1 and the shortening of the C=O bond as compared with TS1". Thus we can picture N,N-DMF molecules approaching the final $1^1A''/1^1A'$ conical intersection with a range of out-of-plane momenta. Those molecules that happen to have near-planar geometries as they reach this region of configuration space will follow the $1^1A''$ path though the conical intersection and dissociate to ground state products. Even in this limit we can envisage a spectrum of outcomes. If the molecule is near planar and has little out-of-plane nuclear motion, then most of the available energy will be released in the form of product translation, and the recoil anisotropy will approach the limiting value given by the axial recoil approximation (in this case $\beta = +2$). Conversely, if the molecule just happens to be near-planar at the relevant point in configuration space but while executing a large amplitude out-of-plane (umbrella-like) vibration, the forces acting during dissociation will lead to rotational and vibrational internal excitation of the product, with a corresponding reduction in its kinetic energy, greater devia-

tion from axial recoil, and a reduction in β. At the other extreme, N,N-DMF molecules that sample the conical intersection at very non-planar geometries will tend to follow the adiabatic path to $N(CH_3)_2[\tilde{X}]$ + $HCO[\tilde{A}]$ products; these products must recoil with much less kinetic energy along trajectories that are much further from the axial recoil limit.

Considering now the photofragment kinetic energy distributions, Figure 6(a) shows the total kinetic energy release (TKER) distribution determined from the momentum distributions in Figure 5, together with the fitted TKER distributions for the 'fast' and 'slow' product channels obtained in the previous experimental study by Forde *et al.*[3]. The distribution peaks at relatively low kinetic energy release, with a mean fraction of the available energy released into translation of $\langle f_T \rangle = 0.30$, but with a long tail that extends out to relatively high energies. This is consistent with excitation of a variety of out-of-plane motions, as discussed above.

Maximum kinetic energy releases for the $HCO[\tilde{X}] + N(CH_3)_2[\tilde{X}]$, $HCO[\tilde{A}]$ + $N(CH_3)_2[\tilde{X}]$, and $HCO[\tilde{X}]$ + $N(CH_3)_2[\tilde{A}]$ channels are 2.53 eV, 1.38 eV, and 0.94 eV, respectively, and are shown as vertical dotted lines on the plot. These have been derived using the N−CO bond strength of 3.89 eV and provisional $N(CH_3)_2$ [$\tilde{A}$-$\tilde{X}$] splitting of 1.59 eV reported by Forde *et al.* [3] and the well-established energy [26] of the $HCO[\tilde{A}]$ state of 1.15 eV.

The TKER distribution obtained from our data is in almost quantitative agreement with the fitted distributions determined by Forde *et al.* [3], but provides no real further insights into the validity or otherwise of the previously proposed decomposition into 'fast' and 'slow' TKER components associated with formation of $\tilde{X}$ and $\tilde{A}$ state $N(CH_3)_2$ fragments. The present

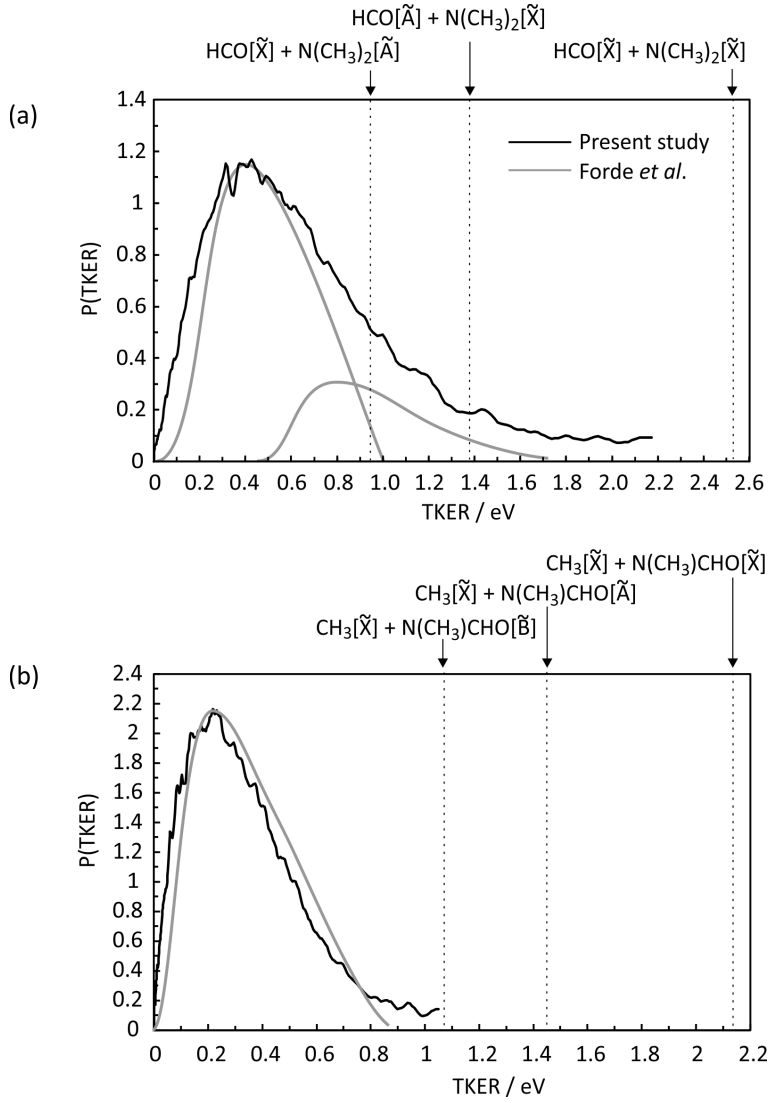

Figure 6: Normalised total kinetic energy release distributions for (a) the N−CO 'peptide' bond fragmentation channel and (b) the N−CH_3 bond fission channel following 193 nm excitation of N,N-DMF. The fitted TKER distributions determined in a previous experimental study by Forde *et al.*[3] are superimposed on the data from the present study. Energetic limits for formation of products in various electronic states are indicated.

data show no obvious discontinuity in either the product yield or the recoil anisotropy (β) parameter in the vicinity of the predicted threshold energies for forming electronically excited products. In our earlier discussion of the observed β parameters in light of the potential energy curves shown in Figure 2(a) we identified motions orthogonal to the N-CO bond extension as likely sources of product internal excitation, and noted opportunities for branching between diabatic potential energy surfaces (and thus for forming different asymptotic products) at both the $2^1A'/1^1A''$ and $1^1A''/1^1A'$ conical intersections. We suggest that the electronic branching in these products remains a somewhat open question, which might be addressable through experiments at other excitation wavelengths (such experiments are currently underway in our laboratory), or by state-of-the-art quantum dynamics simulations.

3.4 N-CH_3 bond cleavage

Of the two products arising from N$-CH_3$ bond cleavage, CH_3 can be ionized at 118 nm, while $HCONCH_3$ cannot. A relatively intense peak corresponding to the CH_3^+ ion is present at $m/z = 15$ in the time-of-flight spectrum (see Figure 3(b)), indicating that the N$-CH_3$ bond cleavage channel is active. As expected, no signal is observed at $m/z = 58$ for the $HCONCH_3$ cofragment.

The velocity-map image for the CH_3 fragment shows a relatively isotropic angular distribution ($\beta = 0.19$). Small values of β can often be explained in terms of a slow or delayed dissociation process. This is unlikely in the present case given both the topology of the calculated potential energy curves and the fact that N$-CH_3$ bond cleavage must be kinetically competitive with

N−CO bond cleavage. Instead, our favoured explanation is that the near-zero value of β arises simply from the molecular geometry. The molecular geometry implies that N−CH_3 bond cleavage will lead to release of a CH_3 fragment at an angle of approximately 60° to the N−CO bond axis. The transition dipole for the dominant $\pi^* \leftarrow \pi$ transition to the $3^1A'$ state lies almost parallel to the N−CO bond axis. In molecules that absorb a photon and dissociate, there will therefore be an approximately $\cos^2$ distribution of the N−CO axis relative to the photolysis laser polarisation vector. A simple model combining this $\cos^2$ distribution of the N−CO bond axis with the (near magic-angle) ejection directions of the CH_3 fragments predicts an almost isotropic distribution of CH_3 photofragments about the laser polarisation axis, as observed.

Figure 6(b) compares the total kinetic energy release distribution determined from the CH_3 velocity-map image with the fitted TKER distribution obtained in the earlier experiments by Forde *et al.*[3]. As for the N−CO channel, the two sets of data, recorded using different experimental techniques, are in remarkably good agreement. Forde *et al.* [3] assigned at least some of their CH_3 signal to cracking products of larger photofragments, particularly $N(CH_3)_2$, resulting from 200 eV electron ionization within their detector. However, we do not believe this to be the case in our experiments, which employ 'soft' 118 nm photoionization. The excess energy of 0.59 eV following 118 nm photoionization of $N(CH_3)_2$ is considerably less than the ~ 3.9 eV [26] required for fragmentation into NCH_3 + CH_3^+ products.

The dotted vertical lines in Figure 6(b) indicate the maximum kinetic energy releases associated with CH_3 partnered by $HCONCH_3$ in its $\tilde{X}$, $\tilde{A}$,

and $\tilde{B}$ states, the three channels predicted by the CASPT2 calculations to be energetically accessible at 193 nm. The measured kinetic energy release distribution does not extend beyond the energetic threshold for formation of $CH_3[\tilde{X}]$ + $HCONCH_3[\tilde{B}]$ products. With reference to the potential energy curves shown in Figure 2(b), it is therefore tempting to suggest that most N,N-DMF($2^1A'$) molecules that dissociate by N−CH_3 bond fission avoid the $2^1A'/1^1A''$ conical intersection at small bond extensions and follow the adiabatic path to electronically excited ($\tilde{B}$ state) $HCONCH_3$ radical products. However, we also recognise that arguments based solely on an observed cut-off in a kinetic energy release spectrum fail if much of the available energy is partitioned into internal excitation of the products. The present data therefore does not exclude the formation of internally excited $\tilde{X}$ or $\tilde{A}$ state $HCONCH_3$ products. Liu *et al.* [4] invoked intersystem crossing to the lowest triplet potential energy surface to explain the formation of CH_3 radical products. However, neither the observed total kinetic energy release data, nor the competitiveness of the N−CH_3 bond fission process with fast N−CO bond fission would appear to sit comfortably with such a mechanism.

3.5 C-H bond cleavage

A photon of wavelength 118 nm provides insufficient energy to ionize atomic hydrogen, but according to the calculated ionization energies reported in Table 1, should suffice to ionize and detect the $CON(CH_3)_2$ cofragment. However, we see no evidence in the time-of-flight spectrum for formation of this product. While secondary dissociation of the $CON(CH_3)_2$ products to CO + $N(CH_3)_2$ is energetically possible at 193 nm, we also see no ev-

idence for the H + $CON(CH_3)_2$ pathway in the H-atom Rydberg tagging photofragment translational spectroscopy experiments. Dissociative ionization of $CON(CH_3)_2$ at 118 nm to form CO^+ + $N(CH_3)_2$ or CO + $N(CH_3)_2^+$ is not energetically possible, so we do not expect to see products from this channel at other masses. We therefore conclude that C-H bond cleavage is too slow to compete with rival photofragmentation pathways following photoexcitation of N,N-DMF at 193 nm. From the potential energy curves shown in Figure 2(c), we see that aldehydic C−H bond fission requires radiationless transfer to the triplet continuum, so the non-observation of these pathways lends further support to the view that intersystem crossing is unlikely to be competitive with the fast rates of N−CO and N−CH_3 bond fission on the singlet potential energy surfaces.

Though we have ruled out the H + $CON(CH_3)_2$ fragmentation pathway, we do detect atomic hydrogen fragments in the H-atom Rydberg tagging photofragment translational spectroscopy measurements described in Section 2.1. The measured H atom flight times t can be converted to a total kinetic energy release distribution using the expression

$$\mathrm{TKER} = \frac{1}{2} m_{\mathrm{H}} \left(1 + \frac{m_{\mathrm{H}}}{m_{\mathrm{R}}}\right) \left(\frac{d}{t}\right)^2 \tag{1}$$

where m_{H} and m_{R} are the masses of the H atom and radical cofragment, and d is the distance between the interaction region and the detector (36.9 cm in the present experiments). We have used $m_{\mathrm{R}} = 72.09$ u, the value appropriate for the radical product formed upon C−H bond fission in N,N-DMF. However, the H atom is so much lighter than any of the possible cofragments that the factor $(1+m_{\mathrm{H}}/m_{\mathrm{R}})$ is always close to unity, and the choice

of cofragment therefore has little effect on the time-of-flight to TKER conversion.

The TKER distribution for H atoms detected following photolysis of N,N-DMF at 193 nm is shown in Figure 7. The distribution comprises a relatively narrow peak centred at ∼0.5 eV and extending beyond 1.5 eV, atop a much broader peak that extends out to beyond 6.0 eV. The low-TKER peak varies little with changes in laser polarisation or wavelength over the range from 193.3 nm to 243.1 nm. This suggests that these H atoms arise either from unimolecular decay of highly internally excited ground-state N,N-DMF formed following internal conversion from the initially excited electronic states, or from unimolecular decay of highly internally excited molecular fragments formed in the primary dissociation process (e.g. the HCO fragments arising from the $N(CH_3)_2$ + HCO channel). The fast component of the distribution extends to kinetic energies far greater than could result from C-H bond fission within either the CHO or CH_3 groups of N,N-DMF, but would be consistent with secondary photolysis of HCO radicals formed in the primary N−CO bond fission process. HCO is known[30] to absorb via the $\tilde{B} \leftarrow \tilde{X}$ transition at 193 nm. The H-CO bond dissociation energy[31] of 0.66±0.04 eV, coupled with the 6.42 eV photon energy, implies an upper limit for the TKER of around 5.76 eV, or higher if the HCO fragments are formed with internal excitation. This value matches well with the observed onset of the broad peak in the TKER distribution derived from the H atom time-of-flight data. The fact that the derived TKER distribution can be rationalised simply in terms of dissociation of internally 'hot' N,N-DMF parent molecules and/or primary molecular fragments, together with sec-

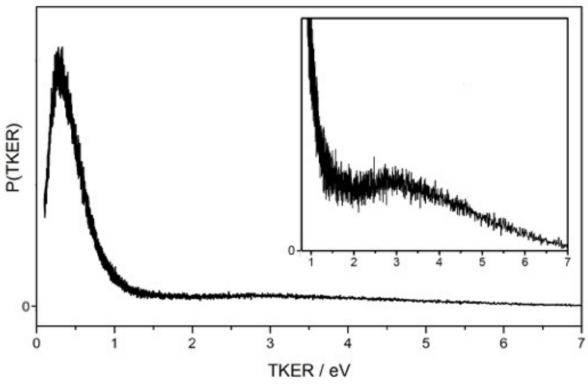

Figure 7: Total kinetic energy release (TKER) distributions derived from measured times-of-flight of H atoms formed in the 193 nm photolysis of N,N-DMF. The inset shows the high-TKER data plotted on an eight-times expanded vertical scale.

ondary photolysis of primary HCO products reinforces the conclusion from the velocity-map imaging study that C-H bond cleavage is not an important primary process in the 193 nm photolysis of N,N-DMF.

4 Conclusions

We have presented data from a comprehensive experimental and theoretical study into the photofragmentation dynamics of N,N-dimethylformamide at 193 nm. In our velocity-map imaging experiments we observe two main fragmentation channels: cleavage of the N−CO 'peptide' bond to form HCO and $N(CH_3)_2$ products; and CH_3 loss. We also see some evidence for H atom formation, with both 'slow' and 'fast' contributions to the H atom system. We tentatively ascribe the slow H atoms as resulting from unimolecular de-

cay of highly vibrationally excited parent N,N-DMF molecules formed by internal conversion from the photoexcited state(s) and/or from predissociation of nascent internally excited HCO. Fast H atoms are thought to result from secondary photolysis of the primary HCO photoproducts. In the case of 'peptide' bond fission, our data are consistent with initial population primarily of the $3^1A'$ state of the parent, followed by sequential internal conversion to the $2^1A'$ and $1^1A''$ states, the latter of which correlates with ground state HCO and $N(CH_3)_2$ products. This has been identified as the dominant fragmentation pathway in two previous theoretical studies [4, 5]. Both studies also identified minor pathways leading to formation of either $N(CH_3)_2$ or HCO in their first electronically excited states. While our measured product total kinetic energy release distributions would certainly be consistent with small contributions from these pathways, we see no clear evidence for them in our data. Our experimental data are in very good agreement with data recorded by Forde *et al.* [3] in their earlier experimental study on N,N-DMF photofragmentation. However, in contrast to the conclusions drawn in the earlier study, we see no need to invoke two different fragmentation pathways in order to explain our observed total kinetic energy release distributions. The products of the N−CO bond fission pathway appear to be formed with significant internal excitation, consistent with rapid impulsive breaking of the bond.

The CH_3 loss channel is also thought to involve a sequence of radiationless transitions following initial population of the $3^1A'$ state, with initial transfer to the $2^1A'$ state followed either by dissociation on this potential energy surface or radiationless transfer to the $1^1A''$ state. The adiabatic

potentials for these two states (see Figure 2) correlate to ground-state CH_3 partnered by $HCONCH_3$ in its second excited [$\tilde{B}$] or ground [$\tilde{X}$] electronic state, respectively. The TKER distribution for this channel does not extend beyond the energetic limit for formation of the $CH_3[\tilde{X}]$ + $HCONCH_3[\tilde{B}]$ products, so would certainly be consistent with dissociation on the $2^1A'$ surface. Dissociation to form ground-state products is also consistent with the data, in which case the measured TKER distribution implies a high degree of product vibrational or rotational excitation.

We see no evidence for direct H atom loss channels from excited-state N,N-DMF in either our velocity-map imaging data or in data from separate H-atom Rydberg tagging photofragment translational spectroscopy measurements. However, as noted above, we do see some evidence for H loss following internal conversion of electronically excited parent or fragment molecules to highly vibrationally excited levels of the respective ground states, as well as observing H atoms from secondary photolysis of HCO fragments formed through N−CO bond fission.

In the future we plan to study N,N-DMF photolysis at additional wavelengths within the ultraviolet, as well as investigating a series of related molecules in order to determine whether the fragmentation pathways observed in the present study are common to other small peptide-bond-containing species.

5 Acknowledgments

We gratefully acknowledge funding via the ERC grant ImageMS and the EPSRC grants EP/G00224X/1 and EP/L005913/1.

References

[1] J. S. Brodbelt, *J. Am. Soc. Mass Spectrom.*, **22**, 197 (2011).

[2] N. R. Forde, T. L. Myers, and L. J. Butler, *Faraday Discuss.*, **108**, 221 (1997).

[3] N. R. Forde, L. J. Butler, and S. A. Abrash, *J. Chem. Phys.*, **110**, 8954 (1999).

[4] D. Liu, W. Fang, Z. Lin, and X. Fu, *J. Chem. Phys.*, **117**, 9241 (2002).

[5] M. Eckert-Maksić and I. Antol, *J. Phys. Chem. A*, **113**, 12582 (2009).

[6] H. D. Hunt and W. T. Simpson, *J. Am. Chem. Soc.*, **75**, 4540 (1953).

[7] K. Kaya and S. Nagakura, *Theoretica Chimica Acta*, **7**, 117 (1967).

[8] L. Serrano-Andrés and M. P. Fülscher, *J. Am. Chem. Soc.*, **118**, 12190 (1996).

[9] R. Liu and P. Pulay, *J. Comp. Chem.*, **13**, 183 (1992).

[10] X. Qiu, Z. Ding, Y. Xu, Y. Wang, and B. Zhang, *Phys. Rev. A*, **89**, 033405 (2014).

[11] W. S. Hopkins, M. L. Lipciuc, S. H. Gardiner, and C. Vallance, *J. Chem. Phys.*, **135**, 034308 (2011).

[12] S. H. Gardiner, T. N. V. Karsili, M. L. Lipciuc, E. Wilman, M. N. R. Ashfold, and C. Vallance, *Phys. Chem. Chem. Phys.*, **16**, 2167 (2014).

[13] A. H. Kung, J. F. Young, and S. E. Harris, *Appl. Phys. Lett.*, **22**, 301 (1973).

[14] A. H. Kung, J. F. Young, and S. E. Harris, *Appl. Phys. Lett.*, **28**, 294 (1976).

[15] N. P. Lockyer and J. C. Vickerman, *Laser Chemistry*, **17**, 139 (1997).

[16] V. Dribinski, A. Ossadtchi, V. A. Mandelshtam, and H. Reisler, *Rev. Sci. Instrum.*, **73** , 2634 (2002).

[17] A. J. T. B. Eppink and D. H. Parker, *Rev. Sci. Instrum.*, **68**, 3477 (1997).

[18] B. Cronin, M. Nix, R. Qadiri, and M. N. R. Ashfold, *Phys. Chem. Chem. Phys.*, **6**, 5031 (2004).

[19] Gaussian 09, Revision A.02, M. J. Frisch, G. W. Trucks, H. B. Schlegel, G. E. Scuseria, M. A. Robb, J. R. Cheeseman, G. Scalmani, V. Barone, G. A. Petersson, H. Nakatsuji, X. Li, M. Caricato, A. Marenich, J. Bloino, B. G. Janesko, R. Gomperts, B. Mennucci, H. P. Hratchian, J. V. Ortiz, A. F. Izmaylov, J. L. Sonnenberg, D. Williams-Young, F. Ding, F. Lipparini, F. Egidi, J. Goings, B. Peng, A. Petrone, T. Henderson, D. Ranasinghe, V. G. Zakrzewski, J. Gao, N. Rega, G. Zheng,

W. Liang, M. Hada, M. Ehara, K. Toyota, R. Fukuda, J. Hasegawa, M. Ishida, T. Nakajima, Y. Honda, O. Kitao, H. Nakai, T. Vreven, K. Throssell, J. A. Montgomery, Jr., J. E. Peralta, F. Ogliaro, M. Bearpark, J. J. Heyd, E. Brothers, K. N. Kudin, V. N. Staroverov, T. Keith, R. Kobayashi, J. Normand, K. Raghavachari, A. Rendell, J. C. Burant, S. S. Iyengar, J. Tomasi, M. Cossi, J. M. Millam, M. Klene, C. Adamo, R. Cammi, J. W. Ochterski, R. L. Martin, K. Morokuma, O. Farkas, J. B. Foresman, and D. J. Fox, Gaussian, Inc., Wallingford CT, 2016.

[20] H. J. Werner, P. J. Knowles, G. Knizia, F. R. Manby, M. Schütz, P. Celani, T. Korona, R. Lindh, A. Mitrushenkov, G. Rauhut, K. R. Shamasundar, T. B. Adler, R. D. Amos, A. Bernhardsson, A. Berning, D. L. Cooper, M. J. O. Deegan, A. J. Dobbyn, F. Eckert, E. Goll, C. Hampel, A. Hesselmann, G. Hetzer, T. Hrenar, G. Jansen, C. Köppl, Y. Liu, A. W. Lloyd, R. A. Mata, A. J. May, S. J. McNicholas, W. Meyer, M. E. Mura, A. Nicklass, D. P. O'Neill, P. Palmieri, K. Pflüger, R. Pitzer, M. Reiher, T. Shiozaki, H. Stoll, A. J. Stone, R. Tarroni, T. Thorsteinsson, M. Wang and A. Wolf, *MOLPRO, version 2010.1, a package of ab initio programs*, 2010.

[21] M. N. R. Ashfold, G. A. King, D. Murdock, M. G. D. Nix, T. A. A. Oliver and A. G. Sage, *Phys. Chem. Chem. Phys.* **12**, 1218 (2010), and references therein.

[22] N. Hobday, M. S. Quinn, K. Nauta, D. U. Andrews, M. J. T. Jordan, and S. H. Kable, *J. Phys. Chem. A*, **46**, 12091 (2013).

[23] C. L. Reed, M. Kono, S. R. Langford, T. W. R. Hancock, R. N. Dixon, and M. N. R. Ashfold, *J. Chem. Phys.*, **106**, 6198 (1997).

[24] C. L. Reed, M. Kono, S. R. Langford, R. N. Dixon, and M. N. R. Ashfold, *J. Chem. Soc. Faraday Trans.*, **93**, 2721 (1997).

[25] R. N. Dixon and T. W. R. Hancock, *J. Phys. Chem.*, **101**, 7567 (1997).

[26] Data from the NIST Chemistry Webbook, http: webbook.nist.gov.

[27] N. R. Forde, L. J. Butler, B. Ruscic, O. Sorkhabi, F. Qi, and A. G. Suits, *J. Chem. Phys.*, **113**, 3088 (2000).

[28] D. H. Mordaunt, M. N. R. Ashfold, and R. N. Dixon, *J. Chem. Phys.*, **104**, 6460 (1996).

[29] R. N. Dixon, *Molecular Physics*, **88**, 949 (1996).

[30] D.E. Milligan and M.E. Jacox, *J. Chem. Phys.*, **51**, 277 (1969).

[31] J. Riedel, S. Dziarzhytski, A. Kuczmann, F. Renth and F. Temps, *Chem. Phys. Lett.*, **414**, 473 (2005).